

# Charged Lepton Flavor Violating processes in Neutrinophilic Higgs+Seesaw model

Naoyuki Haba, Tsuneharu Omija and Toshifumi Yamada

*Graduate School of Science and Engineering, Shimane University, Matsue 690-8504, Japan*

## Abstract

We investigate charged lepton flavor violating (CLFV) processes in the “neutrinophilic Higgs+seesaw model”, in which right-handed neutrinos couple only with an extra Higgs field which develops a tiny vacuum expectation value and the right-handed neutrinos also have Majorana mass. The model realizes a seesaw mechanism around TeV scale without extremely small Dirac Yukawa couplings. A phenomenological feature of the model is CLFV processes induced by loop diagrams of the charged scalar particles and heavy neutrinos. Therefore, first we constrain the model’s parameter space from the search for  $\mu \rightarrow e\gamma$ . Next, we predict the branching ratios of other CLFV processes including the  $\mu \rightarrow 3e$ ,  $\mu + \text{Al} \rightarrow e + \text{Al}$ ,  $\mu + \text{Ti} \rightarrow e + \text{Ti}$ ,  $Z \rightarrow e\mu$ ,  $Z \rightarrow e\tau$ ,  $Z \rightarrow \mu\tau$ ,  $h \rightarrow e\tau$  and  $h \rightarrow \mu\tau$  processes, and discuss their detectability in future experiments.

# 1 Introduction

The origin of the smallness of the neutrino mass is one of the prime open questions in particle physics. One candidate solution to the above mystery is the neutrinophilic Two Higgs Doublet Model [1], where there is an extra Higgs doublet called “neutrinophilic Higgs”) that couples to the lepton doublets and right-handed neutrinos while the coupling of the Standard Model (SM) Higgs doublet to right-handed neutrinos is forbidden by a  $Z_2$  symmetry, and the smallness of the vacuum expectation value (VEV) of the neutrinophilic Higgs explains the smallness of the neutrino mass. In the original proposal [1], Majorana mass for right-handed neutrinos is absent and the neutrinos are purely Dirac particles. However, the  $Z_2$  symmetry that forbids the coupling of the SM Higgs and right-handed neutrinos does not exclude the possibility that right-handed neutrinos have a Majorana mass term. If Majorana mass for right-handed neutrinos is introduced, the model becomes a low-scale realization of the seesaw mechanism [2]-[5], where the smallness of the neutrino mass is accounted for by the seesaw mechanism in addition to the tininess of the neutrinophilic Higgs VEV. We call the new model “neutrinophilic higgs+seesaw model”, for the obvious reason.

Important experimental signatures of the neutrinophilic Higgs+seesaw model are (i) the presence of new scalar particles  $H^\pm, H$  and  $A$  originating dominantly from the neutrinophilic Higgs field, and (ii) charged lepton flavor violating (CLFV) processes, such as  $\mu \rightarrow e\gamma$ , mediated by a loop of the charged scalar  $H^\pm$  and a heavy neutrino. In this paper, we investigate CLFV processes in the neutrinophilic Higgs+seesaw model in detail. First, we constrain the parameter space of the neutrinophilic Higgs+seesaw model from current experimental bounds on CLFV processes, the most stringent bound coming from the  $\mu \rightarrow e\gamma$  decay. Next, we predict branching ratios (or conversion rates) of various CLFV processes and discuss whether it is possible to detect these processes in the future.

Previously, Ref. [6] has studied CLFV processes in the neutrinophilic Two Higgs Doublet Model, but in that work, the Majorana mass term is not considered and the neutrinos are purely Dirac particles. Our work extends it by introducing Majorana mass for right-handed neutrinos. Also, Ref. [7] has studied CLFV processes in a model with similar phenomenological features, but CLFV decays of the SM-like Higgs particle and  $Z$  boson are not included, unlike in our paper.

The rest of the paper is organized as follows. In Section 2, we describe the neutrinophilic Higgs+seesaw model. In Section 3, we give the formulas for the branching ratios of the CLFV process. In Section 4, we present our numerical results, which include the current constraints on the neutrinophilic Higgs+seesaw model and predictions for various CLFV processes. Finally, we summarize our results in Section 5.

## 2 Neutrinophilic Higgs+Seesaw Model

The model contains two Higgs doublet fields,  $H_1$  and  $H_2$ , left-handed leptons,  $\ell_L^\alpha$ , right-handed charged leptons,  $e_R^\alpha$ , and right-handed neutrinos,  $\nu_R^i$ , where  $\alpha = e, \mu, \tau$  is the flavor index for charged leptons and  $i = 1, 2, 3$  is another flavor index. It also contains quarks,  $q_L^k$ ,  $u_R^k$  and  $d_R^k$ , but they play no role in this study. The fields are charged under the SM  $SU(3)_C \times SU(2)_L \times U(1)_Y$  gauge group and a  $Z_2$  symmetry as given in Table 1 (bold numbers indicate the representations).

Table 1: The field content and charge assignments.

Field	$SU(3)_C$	$SU(2)_L$	$U(1)_Y$	$Z_2$
$H_1$	<b>1</b>	<b>2</b>	-1/2	+
$H_2$	<b>1</b>	<b>2</b>	-1/2	-
$\ell_L^\alpha$	<b>1</b>	<b>2</b>	-1/2	+
$e_R^\alpha$	<b>1</b>	<b>1</b>	-1	+
$\nu_R^i$	<b>1</b>	<b>1</b>	0	-
$q_L^k$	<b>3</b>	<b>2</b>	1/6	+
$u_R^k$	<b>3</b>	<b>1</b>	2/3	+
$d_R^k$	<b>3</b>	<b>1</b>	-1/3	+

Note that the above  $Z_2$  charge assignment allows Majorana mass for right-handed neutrinos, while it forbids the Yukawa couplings of SM fermions with  $H_2$  and the Yukawa coupling of right-handed neutrinos with  $H_1$ .

We assume that the  $Z_2$  symmetry is softly broken in the scalar potential. The most general scalar potential and Yukawa couplings are then

$$\begin{aligned}
 -\mathcal{L} = & m_1^2 H_1^\dagger H_1 + m_2^2 H_2^\dagger H_2 - m_3^2 (H_1^\dagger H_2 + H_2^\dagger H_1) \\
 & + \frac{\lambda_1}{2} (H_1^\dagger H_1)^2 + \frac{\lambda_2}{2} (H_2^\dagger H_2)^2 + \lambda_3 (H_1^\dagger H_1)(H_2^\dagger H_2) + \lambda_4 (H_1^\dagger H_2)(H_2^\dagger H_1) + \lambda_5 (H_1^\dagger H_2)^2 + \lambda_5^* (H_2^\dagger H_1)^2 \\
 & + (Y_e)_{\alpha\beta} \ell_L^{\alpha\dagger} \epsilon_g H_1^* e_R^\beta + (Y_D)_{\alpha i} \ell_L^{\alpha\dagger} H_2 \nu_R^i + \frac{1}{2} M_{N_i} \nu_R^{iT} \epsilon_s \nu_R^i + \text{H.c.}, \tag{1}
 \end{aligned}$$

where  $\epsilon_g$  denotes the antisymmetric tensor acting on  $SU(2)_L$  indices and  $\epsilon_s$  denotes that acting on spinor indices. Here, we have taken the flavor basis in which the Majorana mass for right-handed neutrinos is diagonal, and we have made  $m_3^2$  real positive by a phase redefinition. Note that only the  $m_3^2$  term explicitly breaks the  $Z_2$  symmetry, and so the limit with  $m_3^2/m_1^2 \rightarrow 0$

and  $m_3^2/m_2^2 \rightarrow 0$  can be taken naturally at the quantum level. We also assume

$$m_1^2 < 0, \quad m_2^2 > 0, \quad (2)$$

so that  $H_1$  develops a VEV around the scale  $\sqrt{|m_1^2|}$ , and then  $H_2$  gains a VEV through the term  $m_3^2(H_1^\dagger H_2 + H_2^\dagger H_1)$ . Consequently, the VEV of  $H_2$  is proportional to  $m_3^2$  and is controlled by the explicit breaking of the  $Z_2$  symmetry, and therefore the VEV of  $H_2$  can naturally take a small value. Additionally, we assume that  $\lambda_5$  is suppressed as  $|\lambda_5| \ll 8\pi^2 m_\nu |M_k| / |(Y_D)_{\alpha i}|^2 v^2$  and  $|\lambda_5| \ll 8\pi^2 m_\nu m_2^2 / |(Y_D)_{\alpha i}|^2 v^2 |M_k|$ , where  $m_\nu$  denotes the mass scale of active neutrinos and  $v \simeq 246$  GeV. It follows that, unlike the model of Ref. [8], the one-loop correction to the neutrino mass involving  $\lambda_5$  is much smaller than the tree-level mass. The above suppression of  $\lambda_5$  is realized naturally by promoting the  $Z_2$  symmetry to a global  $U(1)$  symmetry under which  $H_2$  is charged by  $+1$ ,  $\nu_R^i$  is charged by  $-1$  and the other fields have no charge and which is broken only softly.

In the neutrinophilic Higgs+seesaw model, we take the limit with  $m_3^2/m_2^2 \rightarrow 0$ . Then, writing the Higgs VEVs as  $\langle H_1^0 \rangle = v_1/\sqrt{2}$  and  $\langle H_2^0 \rangle = v_2/\sqrt{2}$ , we find

$$v_1 \simeq \sqrt{-2m_1^2/\lambda_1}, \quad (3)$$

$$v_2 \simeq \frac{2m_3^2}{m_2^2 + (\lambda_3 + \lambda_4)v_1^2/2} v_1, \quad (4)$$

and hence  $v_2 \ll v_1$ . The physical particles are the lighter CP (Charge conjugation Parity) -even scalar,  $h$ , which is identified with the observed 125 GeV scalar particle, the heavier CP-even scalar,  $H$ , the CP-odd scalar,  $A$ , and the charged scalar,  $H^\pm$ . The masses of  $A$  and  $H^\pm$  are given by

$$m_A^2 = \frac{m_3^2}{\sin \beta \cos \beta}, \quad m_{H^\pm}^2 = \frac{m_3^2}{\sin \beta \cos \beta} - \frac{\lambda_4}{2} v^2 \quad (5)$$

and the masses of  $h$  and  $H$  are given, in the limit with  $v_1 \gg v_2$ , by

$$m_h^2 \simeq \lambda_1 v_1^2, \quad m_H^2 \simeq m_A^2. \quad (6)$$

where  $\tan \beta \equiv v_1/v_2$ . In terms of  $h, H, A, H^\pm$  and would-be Nambu-Goldstone modes  $G^0$  and  $G^\pm$ , the Higgs fields are decomposed as

$$\begin{aligned} H_1 &= \left( \frac{1}{\sqrt{2}} (\sin \beta v + \cos \alpha h + \sin \alpha H - i \sin \beta G^0 - i \cos \beta A) \right. \\ &\quad \left. - \sin \beta G^- - \cos \beta H^- \right), \\ H_2 &= \left( \frac{1}{\sqrt{2}} (\cos \beta v - \sin \alpha h + \cos \alpha H - i \cos \beta G^0 + i \sin \beta A) \right. \\ &\quad \left. - \cos \beta G^- + \sin \beta H^- \right), \end{aligned} \quad (7)$$

where  $\alpha$  is the mixing angle of the CP-even scalars.  $\alpha$  satisfies

$$0 > \alpha > -\frac{\pi}{2}, \quad \tan 2\alpha \simeq -\frac{2}{\tan \beta} \quad (8)$$

in the limit with  $\tan \beta \gg 1$ , and hence  $\alpha \simeq 0$  in the neutrinophilic Higgs+seesaw model.

The interaction of the charged scalar  $H^\pm$  is the dominant source of CLFV processes and is particularly important. The three-point interaction term for  $H^+H^-h$  is given by

$$-\mathcal{L} \supset v\lambda_3 hH^+H^- \quad (9)$$

in the limit with  $\tan \beta \gg 1$ . The Yukawa interaction terms of  $H^\pm$  are

$$-\mathcal{L} \supset -(Y_e)_{\alpha\beta} \nu_L^{\alpha\dagger} e_R^\beta \cos \beta H^+ + (Y_D)_{\alpha i} e_L^{\alpha\dagger} \nu_R^i \sin \beta H^- + \text{H.c.}$$

We turn our attention to the lepton mass. The Dirac and Majorana mass terms are given by

$$-\mathcal{L} \supset \frac{v_1}{\sqrt{2}} (Y_e)_{\alpha\beta} e_L^{\alpha\dagger} e_R^\beta + \frac{v_2}{\sqrt{2}} (Y_D)_{\alpha i} \nu_L^{\alpha\dagger} \nu_R^i + \frac{1}{2} M_{N_i} \nu_R^{iT} \epsilon_s \nu_R^i + \text{H.c.} \quad (10)$$

Then, the mass matrix for neutrinos is obtained as

$$-\mathcal{L} \supset \frac{1}{2} \begin{pmatrix} \nu_L^{\beta T} & \nu_R^{j\dagger} \epsilon_s^T \end{pmatrix} \epsilon_s \begin{pmatrix} O & -\frac{v_2}{\sqrt{2}} (Y_D^*)_{\beta i} \\ -\frac{v_2}{\sqrt{2}} (Y_D^*)_{\alpha j} & \delta_{ij} M_{N_i}^* \end{pmatrix} \begin{pmatrix} \nu_L^\alpha \\ \epsilon_s \nu_R^{i*} \end{pmatrix} + \text{H.c.} \quad (11)$$

The above mass matrix is diagonalized by a unitary matrix,  $U$ , as

$$\begin{pmatrix} O & -\frac{v_2}{\sqrt{2}} (Y_D^*)_{\beta i} \\ -\frac{v_2}{\sqrt{2}} (Y_D^*)_{\alpha j} & \delta_{ij} M_{N_i}^* \end{pmatrix} = U^* \text{diag}(m_{\nu_1}, m_{\nu_2}, m_{\nu_3}, m_{\nu_4}, m_{\nu_5}, m_{\nu_6}) U^\dagger, \quad (12)$$

where  $m_{\nu_1}, m_{\nu_2}$  and  $m_{\nu_3}$  correspond to the tiny active neutrino masses, and  $m_{\nu_4}, m_{\nu_5}$  and  $m_{\nu_6}$  to the masses of heavy neutrinos. We assume  $v_2 \ll M_{N_j}$ . The unitary matrix  $U$  is then approximated by

$$U \simeq \begin{pmatrix} U_{PMNS} & O \\ O & I_3 \end{pmatrix}, \quad (13)$$

where  $U_{PMNS}$  denotes the PMNS (Pontecorvo-Maki-Nakagawa-Sakata) mixing matrix [9, 10] and  $I_3$  denotes the 3-dimensional identity matrix, and we obtain the following seesaw formula:

$$-\frac{v_2^2}{2} (Y_D^*)_{\beta i} (Y_D^*)_{\alpha i} \frac{1}{M_{N_i}} \simeq \left[ U_{PMNS} \begin{pmatrix} m_{\nu_1} & 0 & 0 \\ 0 & m_{\nu_2} & 0 \\ 0 & 0 & m_{\nu_3} \end{pmatrix} U_{PMNS} \right]_{\alpha\beta \text{ component}}. \quad (14)$$

Inverting the relation Eq. (14), one can express the neutrino Dirac Yukawa coupling  $Y_D$  as

$$Y_D = i \frac{\sqrt{2}}{v_2} U_{PMNS} \begin{pmatrix} \sqrt{m_{\nu_1}} & 0 & 0 \\ 0 & \sqrt{m_{\nu_2}} & 0 \\ 0 & 0 & \sqrt{m_{\nu_3}} \end{pmatrix} R_{3 \times 3} \begin{pmatrix} \sqrt{M_{N_1}} & 0 & 0 \\ 0 & \sqrt{M_{N_2}} & 0 \\ 0 & 0 & \sqrt{M_{N_3}} \end{pmatrix} \quad (15)$$

where  $R_{3 \times 3}$  is an arbitrary complex-valued  $3 \times 3$  rotation matrix [11]. The masses of heavy neutrinos are approximated as

$$m_{\nu_4} \simeq M_{N_1}^*, \quad m_{\nu_5} \simeq M_{N_2}^*, \quad m_{\nu_6} \simeq M_{N_3}^*, \quad (16)$$

and the mass eigenstates belonging to  $m_{\nu_4}$ ,  $m_{\nu_5}$  and  $m_{\nu_6}$  are mostly given by the right-handed neutrinos, namely, we find

$$\nu_4 \simeq \epsilon_s \nu_R^{1*}, \quad \nu_5 \simeq \epsilon_s \nu_R^{2*}, \quad \nu_6 \simeq \epsilon_s \nu_R^{3*}. \quad (17)$$

We comment on the constraints from electroweak precision tests. The constraint from the Peskin-Takeuchi  $T$ -parameter [12, 13] can be avoided by taking the coupling constants  $\lambda_4, \lambda_5$  close to 0 so that the charged scalar  $H^\pm$  and the heavy neutral scalars  $H, A$  are nearly mass-degenerate (note  $\beta \simeq \pi/2$ ,  $\alpha \simeq 0$ ). Taking  $\lambda_4 = \lambda_5 = 0$  does not affect the CLFV processes we discuss in the ensuing sections. When  $m_H^2 \simeq m_A^2 \simeq m_{H^\pm}^2$ , the Peskin-Takeuchi  $S$ -parameter is explicitly calculated as

$$S \simeq \frac{1}{6\pi} (2s_W^4 - 2s_W^2 + 1) \times \left\{ -\frac{8}{3} + \frac{8m_{H^\pm}^2}{m_Z^2} + \frac{1}{m_Z^2} \left( 1 - \frac{4m_{H^\pm}^2}{m_Z^2} \right) \sqrt{4m_Z^2 m_{H^\pm}^2 - m_Z^4} \arctan \frac{\sqrt{4m_Z^2 m_{H^\pm}^2 - m_Z^4}}{2m_{H^\pm}^2 - m_Z^2} \right\}. \quad (18)$$

When  $m_H^2 \simeq m_A^2 \simeq m_{H^\pm}^2 = (300 \text{ GeV})^2$ , which will be the benchmark value of our numerical analysis, we get  $S \simeq -0.0003$ . This is consistent with the current experimental bound [14].

Finally, we comment on new physics contributions to the electron electric dipole moment. The two-loop Barr-Zee diagrams that involve  $Y_D$  and contribute to the electron dipole moments are highly suppressed by the coupling of  $H^+$  to quarks (proportional to  $\cos \beta$ ) and also by the mixing of a heavy neutrino with active flavor (proportional to  $Y_D v / M_{N_i}$ ). On the other hand, the one-loop diagrams contributing to the electron dipole moments are proportional to  $\sum_{i=1}^3 (Y_D)_{ei} f_i (Y_D^\dagger)_{ie}$  where  $f_i$  are real constants depending on the heavy neutrino masses. The quantity  $\sum_{i=1}^3 (Y_D)_{ei} f_i (Y_D^\dagger)_{ie}$  is always real and hence no electric dipole moment arises in the model.

### 3 Branching Ratios of Charged Lepton Flavor Violating Processes

The limits with  $m_\ell$  consider the dominant and heavy neutrino

s section. We only charged scalar  $H^\pm$

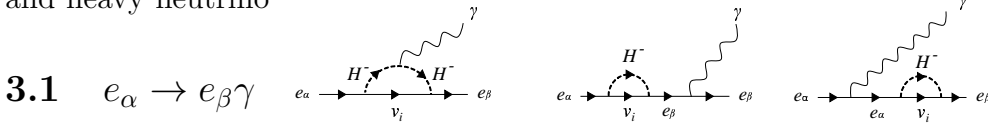


Fig. 1: Feynman diagrams contributing to  $e_\alpha \rightarrow e_\beta \gamma$  at the one-loop level.

CLFV decays of a charged lepton into a charged lepton and a photon,  $e_\alpha \rightarrow e_\beta \gamma$ , arise from the following dipole term, induced by loop diagrams of the charged scalar  $H^\pm$  and heavy neutrinos  $\nu_4, \nu_5, \nu_6$  in Fig. 1:

$$\mathcal{L}_{eff} = \frac{1}{2} e A_D^{\beta\alpha} m_\alpha \bar{e}_\beta \sigma_{\mu\nu} e_\alpha F^{\mu\nu}, \quad (19)$$

$$A_D^{\beta\alpha} = \frac{1}{16\pi^2} \frac{1}{2M_{H^\pm}^2} \sum_{i=1}^3 (Y_D)_{\beta i} F_2(r_i) (Y_D^\dagger)_{i\alpha}, \quad r_i \equiv \frac{M_{N_i}^2}{M_{H^\pm}^2}, \quad (20)$$

$$F_2(x) = \frac{1 - 6x + 3x^2 + 2x^3 - 6x^2 \log x}{6(1-x)^4}. \quad (21)$$

The branching ratio is given by

$$Br(e_\alpha \rightarrow e_\beta \gamma) = 48\pi^3 \frac{\alpha}{G_F^2} |A_D^{\beta\alpha}|^2 Br(e_\alpha \rightarrow e_\beta \nu_\alpha \bar{\nu}_\beta). \quad (22)$$

### 3.2 $e_\alpha \rightarrow e_\beta \bar{e}_\beta e_\beta$

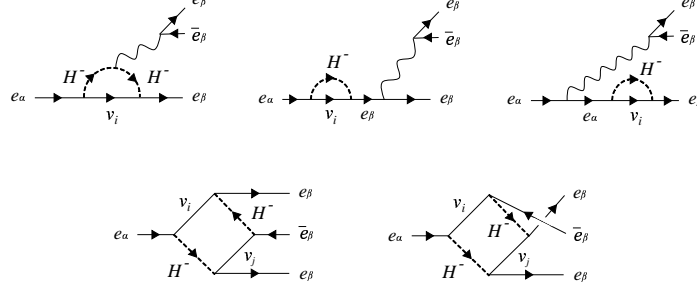


Fig. 2: Feynman diagrams contributing to  $e_\alpha \rightarrow e_\beta \bar{e}_\beta e_\beta$  at the one-loop level. In the upper row are  $\gamma$ -penguin diagrams or  $Z$ -penguin diagrams. However, we neglect the  $Z$ -penguin diagrams in Eq. (29) because they are suppressed by  $m_\alpha m_\beta / M_Z^2$ . In the lower row are Box diagrams.

CLFV decays of a charged lepton into three charged leptons,  $e_\alpha \rightarrow e_\beta \bar{e}_\beta e_\beta$ , arise from the following dipole, non-dipole and box-induced terms, induced by loop diagrams of the charged scalar and heavy neutrinos in Fig. 2:

$$\mathcal{L}_{eff} = \frac{1}{2} e A_D^{\beta\alpha} m_\alpha \bar{e}_\beta \sigma_{\mu\nu} P_R e_\alpha F^{\mu\nu} + e A_{ND}^{\beta\alpha} q^2 \bar{e}_\beta \gamma_\mu P_L e_\alpha A^\mu + e^2 B^{\beta\alpha} (\bar{e}_\beta \gamma_\mu P_L e_\beta) (\bar{e}_\beta \gamma^\mu P_L e_\alpha), \quad (23)$$

$$A_{ND}^{\beta\alpha} = \frac{1}{16\pi^2} \frac{1}{6M_{H^\pm}^2} \sum_{i=1}^3 (Y_D)_{\beta i} G_2(r_i) (Y_D^\dagger)_{i\alpha}, \quad (24)$$

$$e^2 B^{\beta\alpha} = \frac{1}{16\pi^2} \frac{1}{4M_{H^\pm}^2} \sum_{i,j=1}^3 \left\{ \frac{1}{2} (Y_D)_{\beta i} (Y_D^\dagger)_{i\alpha} (Y_D)_{\beta j} (Y_D^\dagger)_{j\beta} D_1(r_i, r_j) + (Y_D^*)_{\beta i} (Y_D^\dagger)_{i\alpha} (Y_D)_{\beta j} (Y_D^T)_{j\beta} \sqrt{r_i r_j} D_2(r_i, r_j) \right\}, \quad (25)$$

$$G_2(x) = \frac{2 - 9x + 18x^2 - 11x^3 + 6x^3 \log x}{6(1-x)^4}, \quad (26)$$

$$D_1(x, y) = -\frac{x^2 \log x}{(1-x)^2(x-y)} - \frac{1}{(1-x)(1-y)} - \frac{y^2 \log y}{(1-y)^2(y-x)}, \quad (27)$$

$$D_2(x, y) = -\frac{x \log x}{(1-x)^2(x-y)} - \frac{1}{(1-x)(1-y)} - \frac{y \log y}{(1-y)^2(y-x)}. \quad (28)$$



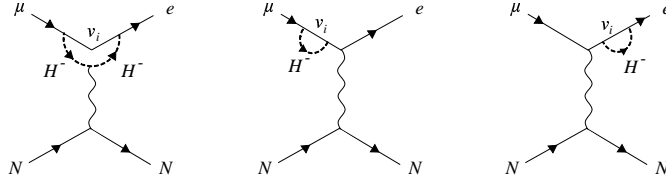
The branching ratio is given by

$$\begin{aligned}
Br(e_\alpha \rightarrow e_\beta \bar{e}_\beta e_\beta) &= 6\pi^2 \frac{\alpha^2}{G_F^2} \left\{ |A_D^{\beta\alpha}|^2 \left( \frac{16}{3} \log \left( \frac{m_\alpha}{m_\beta} \right) - \frac{22}{3} \right) + |A_{ND}^{\beta\alpha}|^2 + \frac{1}{6} |B^{\beta\alpha}|^2 \right. \\
&\quad \left. + \left( -2A_D^{\beta\alpha} A_{ND}^{\beta\alpha*} + \frac{1}{3} A_{ND}^{\beta\alpha} B^{\beta\alpha*} - \frac{2}{3} A_D^{\beta\alpha} B^{\beta\alpha*} + \text{H.c.} \right) \right\} Br(e_\alpha \rightarrow e_\beta \nu_\alpha \bar{\nu}_\beta).
\end{aligned} \tag{29}$$

Here, the contribution from the  $Z$ -penguin diagram is neglected because it is suppressed by  $m_\alpha m_\beta / M_Z^2$  compared to the  $\gamma$ -penguin diagram.

### 3.3 $\mu N \rightarrow e N$

The  $\mu \rightarrow e$  conversion is dominated by the non-dipole term  $A_N$



and the dipole term  $A_D$  and the  $eN$  in Fig. 3.

Fig. 3: Feynman diagrams contributing to  $\mu N \rightarrow e N$  at the one-loop level. They are  $\gamma$ -penguin diagrams or  $Z$ -penguin diagrams. However, we neglect the  $Z$ -penguin diagrams in Eq. (30) because they are suppressed by  $m_\alpha m_\beta / M_Z^2$ . In addition, the Higgs-penguin diagram is neglected because the up and down quark Yukawa couplings are tiny.

The conversion rate divided by the muon capture rate,  $CR(\mu \rightarrow e)$ , reads

$$CR(\mu \rightarrow e) = \frac{1}{\Gamma_{\text{capture}}} \frac{p_e E_e m_\mu^3 \alpha^3 G_F^2}{8\pi^2 Z} Z_{eff}^4 F_p^2 \left| (Z + N)g_{LV}^{(0)} + (Z - N)g_{LV}^{(1)} \right|^2, \tag{30}$$

$$g_{LV}^{(0)} = \frac{1}{2} \sum_{q=u,d} \left( g_{LV}^{(q)} G_V^{(q,p)} + g_{LV}^{(q)} G_V^{(q,n)} \right), \quad g_{LV}^{(1)} = \frac{1}{2} \sum_{q=u,d} \left( g_{LV}^{(q)} G_V^{(q,p)} - g_{LV}^{(q)} G_V^{(q,n)} \right), \tag{31}$$

$$g_{LV}^{(q)} = \frac{\sqrt{2}}{G_F} e^2 Q_q (A_{ND}^{\mu e} - A_D^{\mu e}), \tag{32}$$

where  $p_e$  and  $E_e$  are the momentum and energy of the final state electron, and  $Z$  and  $N$  are the number of protons and neutrons, respectively.  $Z_{eff}$  is the effective atomic charge,  $F_p$  is the nuclear matrix element, and  $g_{LV}^{(0)}, g_{LV}^{(1)}$  are effective charges.  $\Gamma_{\text{capture}}$  denotes the muon capture rate, and  $Q_q$  is the electric charge of quark  $q$ . Here, the contribution from the  $Z$ -penguin diagram is again neglected, and that from the Higgs-penguin diagram is neglected because the up

and down quark Yukawa couplings are tiny. Also, since  $\cos \beta \simeq 0$ , box diagrams involving two quarks and two leptons

### 3.4 $Z \rightarrow \bar{e}_\alpha e_\beta$

CLFV decays of a  $Z$  contributing to  $Z \rightarrow \bar{e}_\alpha e_\beta$  -

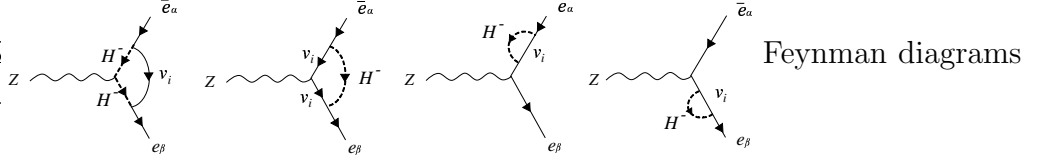


Fig. 4: Feynman diagrams contributing to  $Z \rightarrow \bar{e}_\alpha e_\beta$  at the one-loop level.

In the leading order of  $M_Z^2/M_{H^\pm}^2$ , the effective Lagrangian contributing to  $Z \rightarrow \bar{e}_\alpha e_\beta$  decay is given by

$$\mathcal{L}_{eff} = -A_{ND}^{\beta\alpha} \left( -\frac{1}{2} + \sin^2 \theta_W \right) g_Z \bar{e}_\beta \gamma_\mu P_L e_\alpha Z^\mu. \quad (33)$$

The branching ratio for  $Z \rightarrow \bar{e}_\alpha e_\beta$  is

$$Br(Z \rightarrow \bar{e}_\alpha e_\beta) = Br(Z \rightarrow \bar{e}_\alpha e_\alpha) \frac{g_{eL}^2}{g_{eL}^2 + g_{eR}^2} M_Z^4 \left| A_{ND}^{\beta\alpha} \right|^2, \quad (34)$$

1

### 3.5 $h \rightarrow \bar{e}_\alpha e_\beta$

We show Feynman

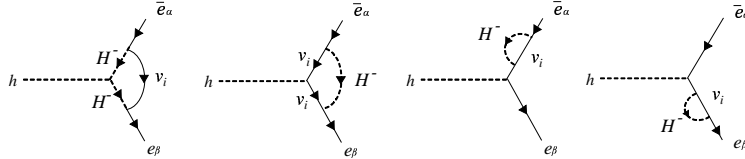


Fig. 5: Feynman diagrams contributing to  $h \rightarrow \bar{e}_\alpha e_\beta$  at the one-loop level.

In the leading order of  $m_h^2/M_{H^\pm}^2$ , the effective Lagrangian contributing to  $h \rightarrow \bar{e}_\alpha e_\beta$  decay is given by

$$\mathcal{L}_{eff} = \frac{1}{16\pi^2} \frac{\lambda_3 v m_\alpha}{M_{H^\pm}^2} \sum_{i=1}^3 (Y_D)_{\beta i} G_H(r_i) (Y_D^\dagger)_{i\alpha} \bar{e}_\beta P_R e_\alpha h, \quad (35)$$

$$G_H(x) = \frac{1 - 4x + 3x^2 - 2x^2 \log x}{4(1-x)^3}, \quad (36)$$

where  $\lambda_3$  is the scalar quartic coupling that appears in Eq. (1).  $G_H$  is a novel function different from  $F_2$  in  $A_D$  or  $G_2$  in  $A_{ND}$ . The branching ratio for  $h \rightarrow \bar{e}_\alpha e_\beta$  is

$$Br(h \rightarrow \bar{e}_\alpha e_\beta) = Br(h \rightarrow \bar{e}_\alpha e_\alpha) \frac{1}{2} \left| \frac{1}{16\pi^2} \frac{1}{M_{H^\pm}^2} \frac{\lambda_3 v^2}{\sqrt{2}} \sum_{i=1}^3 (Y_D)_{\beta i} G_H(r_i) (Y_D^\dagger)_{i\alpha} \right|^2. \quad (37)$$

## 4 Numerical Study

We investigate CLFV processes in the neutrinophilic Higgs+seesaw model, based on the branching ratio formulas in Sect. 3. First, we use current experimental upper limits on CLFV branching ratios to constrain the parameters of the model. Next, under the above constraint, we predict the branching ratios of various CLFV processes including  $\mu \rightarrow 3e$ ,  $\mu + \text{Al} \rightarrow e + \text{Al}$ ,  $\mu + \text{Ti} \rightarrow e + \text{Ti}$ ,  $Z \rightarrow e\mu$ ,  $Z \rightarrow e\tau$ ,  $Z \rightarrow \mu\tau$ ,  $h \rightarrow \mu\tau$  and  $h \rightarrow e\tau$ , and assess their detectability in the future.

### 4.1 Assumptions on the Model Parameters

The branching ratio formulas of CLFV processes depend on the neutrino Dirac Yukawa matrix Eq. (15), the charged scalar mass  $m_{H^\pm}$  and the right-handed neutrino Majorana masses  $M_{N_1}$ ,  $M_{N_2}$  and  $M_{N_3}$ . The neutrino Dirac Yukawa matrix depends on  $v_2$ ,  $M_{N_1}$ ,  $M_{N_2}$ ,  $M_{N_3}$ ,  $m_{\nu_1}$ ,  $m_{\nu_2}$ ,  $m_{\nu_3}$  and  $U_{PMNS}$  as well as a complex-valued  $3 \times 3$  rotation matrix  $R_{3 \times 3}$ . There are too many parameters and it is not easy to gain physical insight to the phenomenology of the model. Therefore, we reduce the number of parameters by considering the following situation.

For the charged scalar mass  $m_{H^\pm}$ , the most phenomenologically interesting situation is when the charged scalar particle is detectable at the LHC. Hence, we assume

$$m_{H^\pm} = 0.3 \text{ TeV}. \quad (38)$$

For the tiny active neutrino masses  $m_{\nu_1}$ ,  $m_{\nu_2}$  and  $m_{\nu_3}$ , we consider both Normal Hierarchy (NH) and Inverse Hierarchy (IH) cases, while focusing on the case where the lightest neutrino mass is 0; namely, we assume

$$m_{\nu_1} = 0 \text{ (NH)}, m_{\nu_3} = 0 \text{ (IH)} \quad (39)$$

The values of  $m_{\nu_2}$  and  $m_{\nu_3}$  ( $m_{\nu_1}$  and  $m_{\nu_2}$ ) in the NH (IH) case are obtained from the mass differences measured in neutrino oscillation experiments. In this paper, we employ the central values of the mass differences given in NuFIT 4.1 [15, 16].

For the parameters of  $U_{PMNS}$ , we employ the central values of the three mixing angles in NuFIT 4.1 [15, 16]. As benchmark values of the Dirac phase  $\delta$ , we take the  $3\sigma$  bounds and central value in the NuFIT 4.1 result [15, 16] as

$$\delta = 144^\circ, 221^\circ, 357^\circ \text{ (NH)} \quad (40)$$

$$\delta = 205^\circ, 282^\circ, 348^\circ \text{ (IH)} \quad (41)$$

We set the Majorana phase to be 0.

For the Majorana masses of right-handed neutrinos, we assume them to be degenerate as

$$M_{N_1} = M_{N_2} = M_{N_3} = M_N, \quad (42)$$

where  $M_N$  is taken as real positive by a phase redefinition. We have found numerically that the branching ratios of CLFV processes do not change significantly even when the Majorana masses are hierarchical as  $M_{N_1} = 0.1M_N$ ,  $M_{N_2} = M_{N_3} = M_N$  or  $M_{N_1} = M_{N_2} = 0.1M_N$  and  $M_{N_3} = M_N$ .

For the neutrinophilic Higgs VEV  $v_2$ , we take it to be proportional to  $\sqrt{M_N}$  as

$$v_2 = 1 \times 10^{-6} \times \sqrt{\frac{M_N}{\text{TeV}}} \text{ TeV (NH)}, \quad (43)$$

$$v_2 = 2 \times 10^{-6} \times \sqrt{\frac{M_N}{\text{TeV}}} \text{ TeV (IH)}. \quad (44)$$

These values of  $v_2$  ensure  $|Y_D| \sim 0.05$  in each hierarchy, where we have defined  $|Y_D|$  as the minimum absolute value of the Yukawa matrix components when  $\text{Im}\theta_1 = \text{Im}\theta_2 = \text{Im}\theta_3 = 0$ . Note that the motivation for the neutrinophilic Higgs+seesaw model is to realize low-scale seesaw without taking very small values for the neutrino Dirac Yukawa coupling, hence it is essential to have  $|Y_D|$  not much smaller than 1.

For  $R_{3 \times 3}$ , we parametrize it in terms of three complex rotation angles  $\theta_j = \text{Re}\theta_j + i\text{Im}\theta_j$  ( $j = 1, 2, 3$ ) as

$$R_{3 \times 3} = \begin{pmatrix} 1 & 0 & 0 \\ 0 & \cos \theta_1 & -\sin \theta_1 \\ 0 & \sin \theta_1 & \cos \theta_1 \end{pmatrix} \begin{pmatrix} \cos \theta_2 & 0 & -\sin \theta_2 \\ 0 & 1 & 0 \\ \sin \theta_2 & 0 & \cos \theta_2 \end{pmatrix} \begin{pmatrix} \cos \theta_3 & -\sin \theta_3 & 0 \\ \sin \theta_3 & \cos \theta_3 & 0 \\ 0 & 0 & 1 \end{pmatrix} \quad (45)$$

For the sake of simplifying the analysis, we vary each  $\theta_j$  separately while fixing the other complex angles at zero. When we vary each  $\theta_j$ , its real part  $\text{Re}\theta_j$  does not affect the branching ratios of CLFV processes, which is understood as follows: Let us focus on the case where we vary  $\theta_1$  while fixing  $\theta_2 = \theta_3 = 0$ .  $R_{3\times 3}$  can then be decomposed as

$$R_{3\times 3} = \begin{pmatrix} 1 & 0 & 0 \\ 0 & \cos(i\text{Im}\theta_1) & -\sin(i\text{Im}\theta_1) \\ 0 & \sin(i\text{Im}\theta_1) & \cos(i\text{Im}\theta_1) \end{pmatrix} \begin{pmatrix} 1 & 0 & 0 \\ 0 & \cos(\text{Re}\theta_1) & -\sin(\text{Re}\theta_1) \\ 0 & \sin(\text{Re}\theta_1) & \cos(\text{Re}\theta_1) \end{pmatrix}. \quad (46)$$

Since we are assuming that the Majorana masses are degenerate as Eq. (42), the matrix with  $\text{Re}\theta_1$  in Eq. (46) cancels in the combination  $\sum_{i=1}^3 (Y_D)_{\beta i} f(r_i) (Y_D^\dagger)_{i\alpha}$  where  $f$  is any function and  $r_i = M_{N_i}^2 / M_{H^\pm}^2$ . Therefore, we only regard the imaginary parts  $\text{Im}\theta_1$ ,  $\text{Im}\theta_2$  and  $\text{Im}\theta_3$  as the parameters of  $R_{3\times 3}$ . The larger the absolute value of  $\text{Im}\theta_j$  is, the larger  $Y_D$  becomes. Thus, to maintain perturbativity, we restrict the range as  $-2 < \text{Im}\theta_j < 2$ .

The above are our assumptions on the model parameters. Consequently, for one CLFV process such as  $\mu \rightarrow 3e$ , we show 18 plots on  $(M_N, \text{Im}\theta_j)$ -parameter space [ $3 (\delta) \times 3 (\text{Im}\theta) \times 2 (\text{NH, IH}) = 18$ ].

## 4.2 Constraints on the Neutrinophilic Higgs+Seesaw Model from Charged Lepton Flavor Violating Processes

The CLFV processes experimentally searched for are  $e_\alpha \rightarrow e_\beta \gamma$ ,  $e_\alpha \rightarrow 3e_\beta$ ,  $\mu N \rightarrow e N$ ,  $Z \rightarrow \bar{e}_\alpha e_\beta$  and  $h \rightarrow \bar{e}_\alpha e_\beta$ . For each process, the upper limit on the branching ratio (or conversion rate) is obtained by experiments and it constrains the model parameter space. At present, the strongest constraint comes from the upper limit on the  $\mu \rightarrow e \gamma$  branching ratio,  $Br(\mu \rightarrow e \gamma) < 4.2 \times 10^{-13}$  [17], in the entire parameter space. Therefore, in the study of the current experimental constraints, we can concentrate on the  $\mu \rightarrow e \gamma$  process while neglecting bounds from other CLFV processes [18]-[21].

The constraint on the  $(M_N, \text{Im}\theta_j)$ -parameter space from the bound  $Br(\mu \rightarrow e \gamma) < 4.2 \times 10^{-13}$  is displayed by the blue solid line in every figure, for both NH and IH, for  $m_{H^\pm} = 0.3$  TeV,  $v_2 = 1 (2) \times 10^{-6} \times \sqrt{\frac{M}{\text{TeV}}}$  TeV in NH (IH), and for the benchmark values of the Dirac phase  $\delta$ . Additionally, we show the constraint when  $v_2$  is multiplied by 1/3 and thus  $Y_D$  is uniformly multiplied by 3, by the dashed blue line.

We observe that the constraint tends to be weaker for smaller  $M_N$  and  $|\text{Im}\theta_j|$ . This is because  $Y_D$  is proportional to  $\sqrt{M_N}$  and  $R_{3\times 3}$  (see Eq. (15)), and so  $Br(\mu \rightarrow e \gamma)$  is suppressed for small  $M_N$  and  $|\text{Im}\theta_j|$ .

## 4.3 Prediction on Charged Lepton Flavor Violating Processes

### 4.3.1 $\mu \rightarrow 3e$

Among the  $e_\alpha \rightarrow e_\beta \bar{e}_\beta e_\beta$  processes, the future sensitivity for the  $\mu \rightarrow 3e$  decay reaches  $Br(\mu \rightarrow 3e) = 10^{-16}$  [22] and so there is a large chance that this mode is detected even when the model satisfies the current experimental bound on  $Br(\mu \rightarrow e\gamma)$ . Therefore, we show in Fig. 6 (Normal Hierarchy) and Fig. 7 (Inverse Hierarchy) the prediction on  $Br(\mu \rightarrow 3e)$ , along with the value of  $Br(\mu \rightarrow e\gamma)$ .

In Fig. 6, the blue solid line agrees with  $Br(\mu \rightarrow e\gamma) = 4.2 \times 10^{-13}$  for NH and  $v_2$  in Eq. (43), and the region to the left of the blue solid line is excluded by the search for  $\mu \rightarrow e\gamma$ . The green solid line agrees with  $Br(\mu \rightarrow 3e) = 10^{-16}$ , the future sensitivity. Therefore, in the region between the blue solid line and the green solid line, the  $\mu \rightarrow 3e$  process can be detected in the future. Figure 7 is the corresponding figure for IH and  $v_2$  in Eq. (44).

In the same figures, the blue and green dashed lines are contours of  $Br(\mu \rightarrow e\gamma) = 4.2 \times 10^{-13}$  and  $Br(\mu \rightarrow 3e) = 10^{-16}$  in the case when  $v_2$  is multiplied by 1/3 and thus  $Y_D$  is uniformly multiplied by 3 according to Eq. (15). Since the dipole and non-dipole terms  $A_D, A_{ND}$  are proportional to  $Y_D^2$  whereas the box-induced term  $B$  is proportional to  $Y_D^4$ , reducing  $v_2$  affects  $Br(\mu \rightarrow 3e)$  and  $Br(\mu \rightarrow e\gamma)$  differently. However, such an effect is not clearly seen in the figures, as the region between the blue and green dashed lines has a similar size to that between the blue and green solid lines.

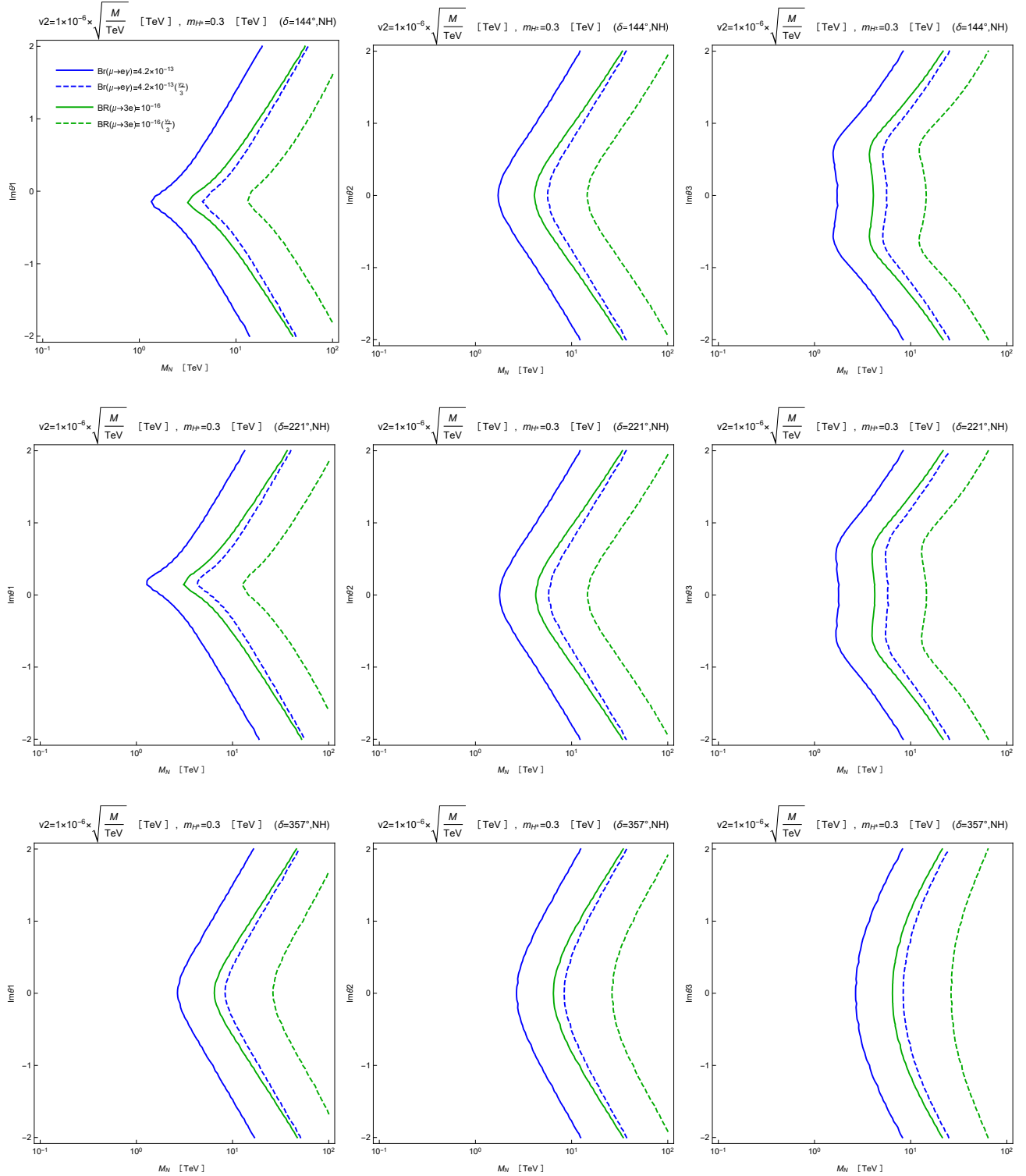


Fig. 6: Prediction for  $Br(\mu \rightarrow 3e)$ , along with the values of  $Br(\mu \rightarrow e\gamma)$ . The neutrino mass hierarchy is Normal Hierarchy, and we fix  $m_{H^\pm} = 0.3$  TeV. We take  $\delta = 144^\circ, 221^\circ$  and  $357^\circ$  in the first, second and third rows. In the first column, we vary  $\text{Im}\theta_1 \neq 0$  while fixing  $\text{Im}\theta_2 = \text{Im}\theta_3 = 0$ . In the second column, we vary  $\text{Im}\theta_2 \neq 0$  while fixing  $\text{Im}\theta_1 = \text{Im}\theta_3 = 0$ . In the third column, we vary  $\text{Im}\theta_3 \neq 0$  while fixing  $\text{Im}\theta_1 = \text{Im}\theta_2 = 0$ . The blue solid line corresponds to  $Br(\mu \rightarrow e\gamma) = 4.2 \times 10^{-13}$  for  $v_2$  in Eq. (43), and the region on the left of the blue solid line is excluded by the search for  $Br(\mu \rightarrow e\gamma)$ . The green solid line corresponds to  $Br(\mu \rightarrow 3e) = 10^{-16}$ , the future sensitivity, for  $v_2$  in Eq. (43). The blue dashed line corresponds to  $Br(\mu \rightarrow e\gamma) = 4.2 \times 10^{-13}$  and the green dashed line corresponds to  $Br(\mu \rightarrow 3e) = 10^{-16}$  in the case when  $v_2$  is multiplied by  $1/3$  and thus  $Y_D$  is uniformly multiplied by 3.

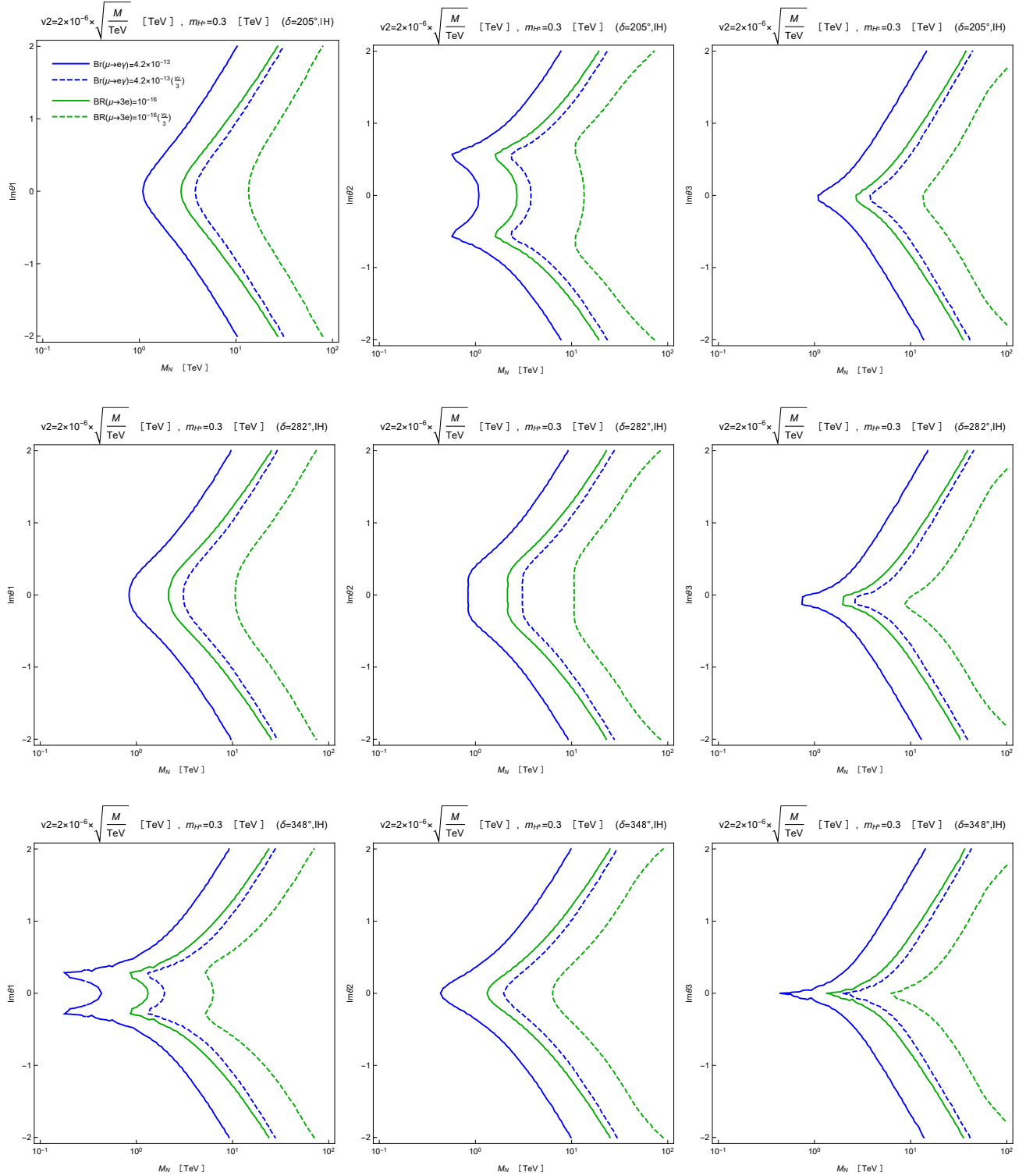


Fig. 7: Same as figure 6 except that the neutrino mass hierarchy is Inverted Hierarchy and  $v_2$  is given in Eq. (44).



### 4.3.2 $\mu$ - $e$ Conversions

The processes whose sensitivity will be improved in the future are the  $\mu + \text{Al} \rightarrow e + \text{Al}$  and  $\mu + \text{Ti} \rightarrow e + \text{Ti}$  processes. The future sensitivity for  $CR(\mu + \text{Al} \rightarrow e + \text{Al})$  is  $2 \times 10^{-17}$  [23], and that for  $CR(\mu + \text{Ti} \rightarrow e + \text{Ti})$  is  $10^{-18}$  [6]. Therefore, we study whether the  $\mu + \text{Al} \rightarrow e + \text{Al}$  and  $\mu + \text{Ti} \rightarrow e + \text{Ti}$  processes can be detected in the future. In the numerical calculation of the conversion rates, we employ the values of  $Z_{eff}$ ,  $F_p$ ,  $\Gamma_{\text{capture}}$  from Ref. [24].

We comment that a peculiar property of the conversion rates  $CR(\mu N \rightarrow e N)$  is that they are zero if  $M_N = m_{H^\pm}$ , because  $A_{ND} = A_D$  at  $\frac{M_N^2}{M_{H^\pm}^2} = 1$ . Therefore, the plots of  $CR(\mu + \text{Al} \rightarrow e + \text{Al})$  and  $CR(\mu + \text{Ti} \rightarrow e + \text{Ti})$  show a different behavior from other processes around the region  $M_N \simeq m_{H^\pm} = 0.3$  TeV. However, this region is excluded by the  $\mu \rightarrow e\gamma$  search and so such a behavior is unimportant.

In Fig. 8, the solid orange line agrees with  $CR(\mu + \text{Al} \rightarrow e + \text{Al}) = 2 \times 10^{-17}$ , the future sensitivity, for NH and  $v_2$  in Eq. (43). Therefore, in the region between the solid blue line and the solid orange line (we neglect the orange line near  $M_N = 0.3$  TeV), the  $\mu + \text{Al} \rightarrow e + \text{Al}$  process can be detected in the future. Figure 9 is the corresponding plot for IH and  $v_2$  in Eq. (44).

In the same figures, the dashed orange line agrees with  $CR(\mu + \text{Al} \rightarrow e + \text{Al}) = 2 \times 10^{-17}$  when  $v_2$  is multiplied by  $1/3$ , and the  $\mu + \text{Al} \rightarrow e + \text{Al}$  process can be detected in the region between the dashed blue line and the dashed orange line for this  $v_2$ . Since the dipole and non-dipole operators  $A_D, A_{ND}$  are both proportional to  $Y_D^2$ ,  $Br(\mu \rightarrow e\gamma)$  and  $CR(\mu + \text{Al} \rightarrow e + \text{Al})$  both scale with  $1/v_2^4$ . Hence, the relative location of the contours of  $Br(\mu \rightarrow e\gamma)$  and  $CR(\mu + \text{Al} \rightarrow e + \text{Al})$  does not depend on  $v_2$ .

In Fig. 10, the solid purple line agrees with  $CR(\mu + \text{Ti} \rightarrow e + \text{Ti}) = 10^{-18}$ , the future sensitivity, for NH and  $v_2$  in Eq. (43). Therefore, in the region between the solid blue line and the solid purple line (we neglect the purple line near  $M_N = 0.3$  TeV), the  $\mu + \text{Ti} \rightarrow e + \text{Ti}$  process can be detected in the future. Figure 11 is the corresponding plot for IH and  $v_2$  in Eq. (44).

In the same figures, the dashed purple line agrees with  $CR(\mu + \text{Ti} \rightarrow e + \text{Ti}) = 10^{-18}$  when  $v_2$  is multiplied by  $1/3$ , and the  $\mu + \text{Ti} \rightarrow e + \text{Ti}$  process can be detected in the region between the dashed blue line and the dashed purple line for this  $v_2$ . Just as with Al, the relative location of the contours of  $Br(\mu \rightarrow e\gamma)$  and  $CR(\mu + \text{Ti} \rightarrow e + \text{Ti})$  does not depend on  $v_2$ .

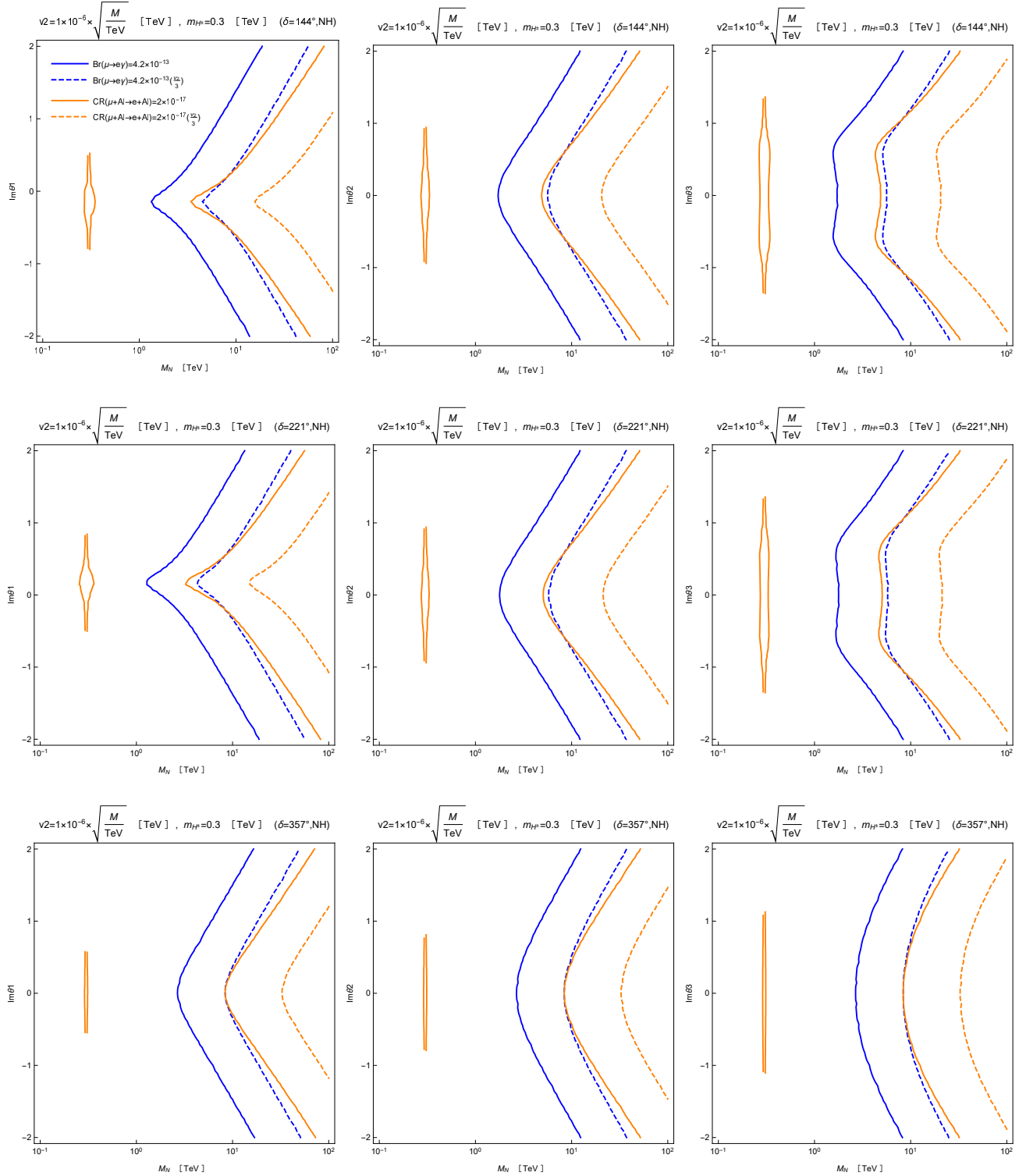


Fig. 8: Prediction for  $CR(\mu + Al \rightarrow e + Al)$ , along with the values of  $Br(\mu \rightarrow e\gamma)$ . The neutrino mass hierarchy is Normal Hierarchy, and we fix  $m_{H\pm} = 0.3$  TeV. We take  $\delta = 144^\circ, 221^\circ$  and  $357^\circ$  in the first, second and third rows. In the first column, we vary  $Im\theta_1 \neq 0$  while fixing  $Im\theta_2=Im\theta_3 = 0$ . In the second column, we vary  $Im\theta_2 \neq 0$  while fixing  $Im\theta_1=Im\theta_3 = 0$ . In the third column, we vary  $Im\theta_3 \neq 0$  while fixing  $Im\theta_1=Im\theta_2 = 0$ . The solid blue line corresponds to  $Br(\mu \rightarrow e\gamma) = 4.2 \times 10^{-13}$  for  $v_2$  in Eq. (43), and the region on the left of the solid blue line is excluded by the search for  $Br(\mu \rightarrow e\gamma)$ . The solid orange line corresponds to  $CR(\mu + Al \rightarrow e + Al) = 2 \times 10^{-17}$ , the future sensitivity, for  $v_2$  in Eq. (43). The dashed blue line corresponds to  $Br(\mu \rightarrow e\gamma) = 4.2 \times 10^{-13}$  and the dashed orange line corresponds to  $CR(\mu + Al \rightarrow e + Al) = 2 \times 10^{-17}$  when  $v_2$  is multiplied by  $1/3$ .

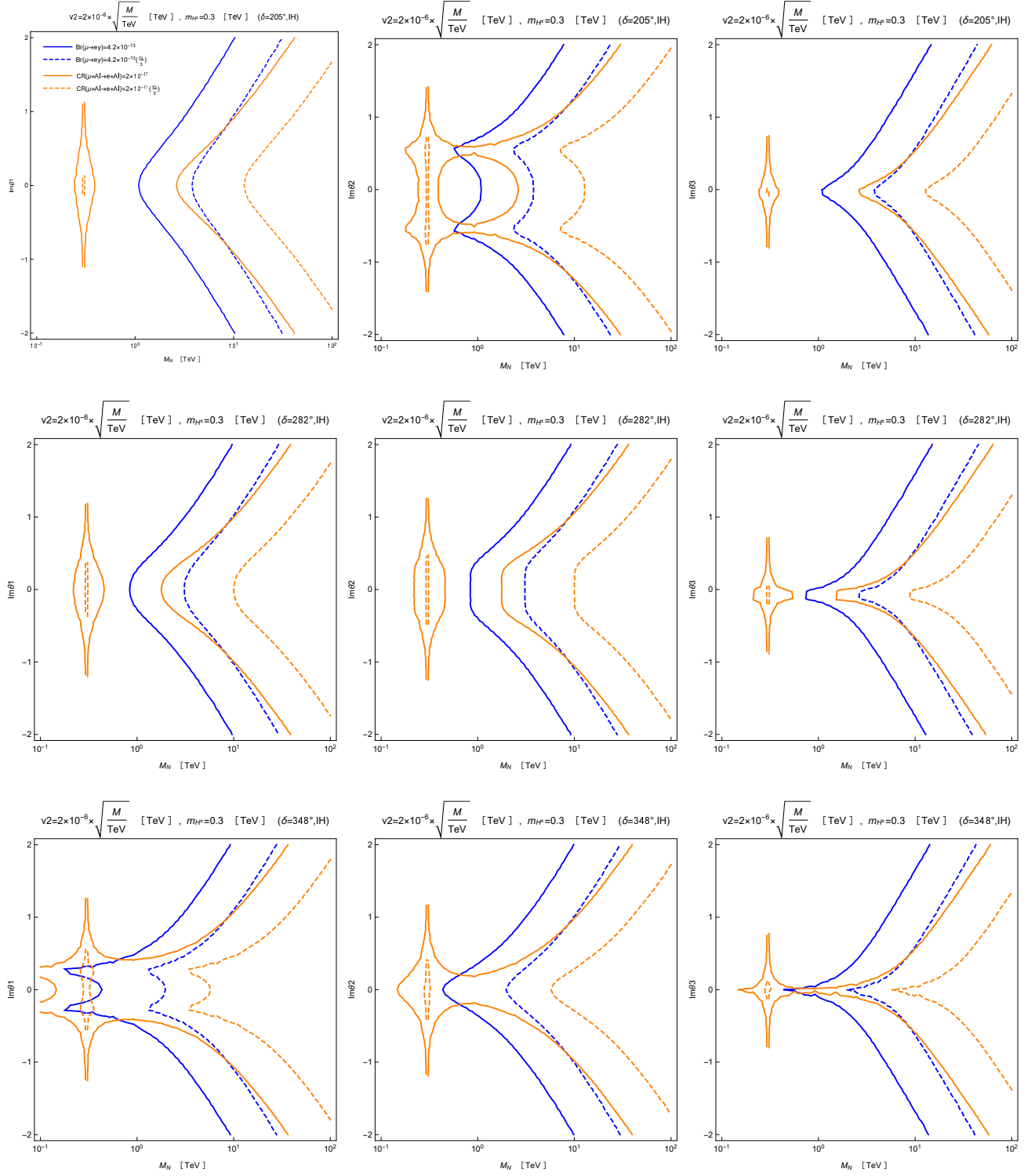


Fig. 9: Same as figure 8 except that the neutrino mass hierarchy is Inverted Hierarchy and  $v_2$  is given in Eq. (44).

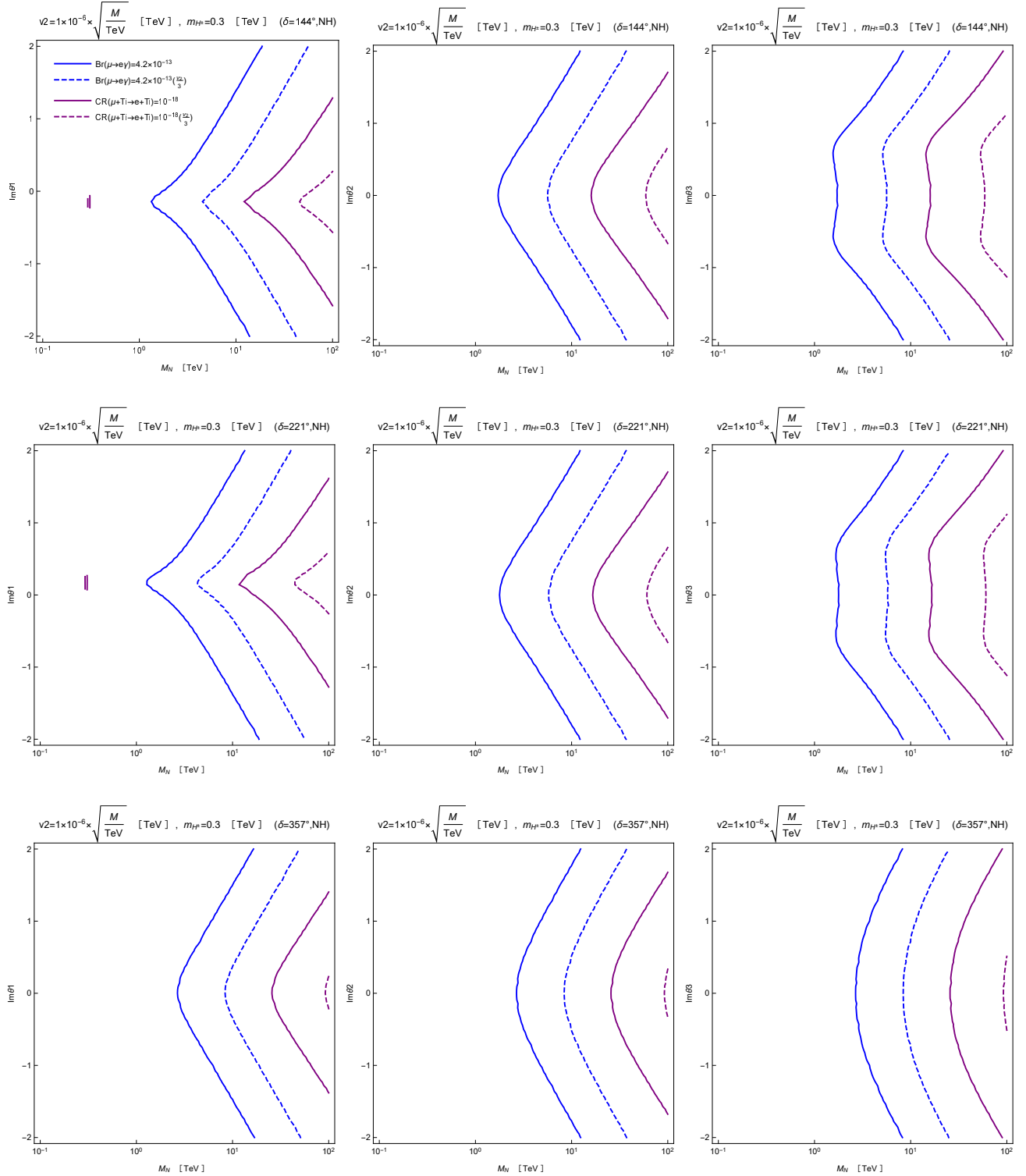


Fig. 10: Same as figure 8 except that the prediction for  $CR(\mu + \text{Ti} \rightarrow e + \text{Ti})$  is presented by the purple lines, for Normal Hierarchy. The solid purple line corresponds to  $CR(\mu + \text{Ti} \rightarrow e + \text{Ti}) = 10^{-18}$  for  $v_2$  in Eq. (43), and the dashed purple line corresponds to  $CR(\mu + \text{Ti} \rightarrow e + \text{Ti}) = 10^{-18}$  when  $v_2$  is multiplied by  $1/3$ .

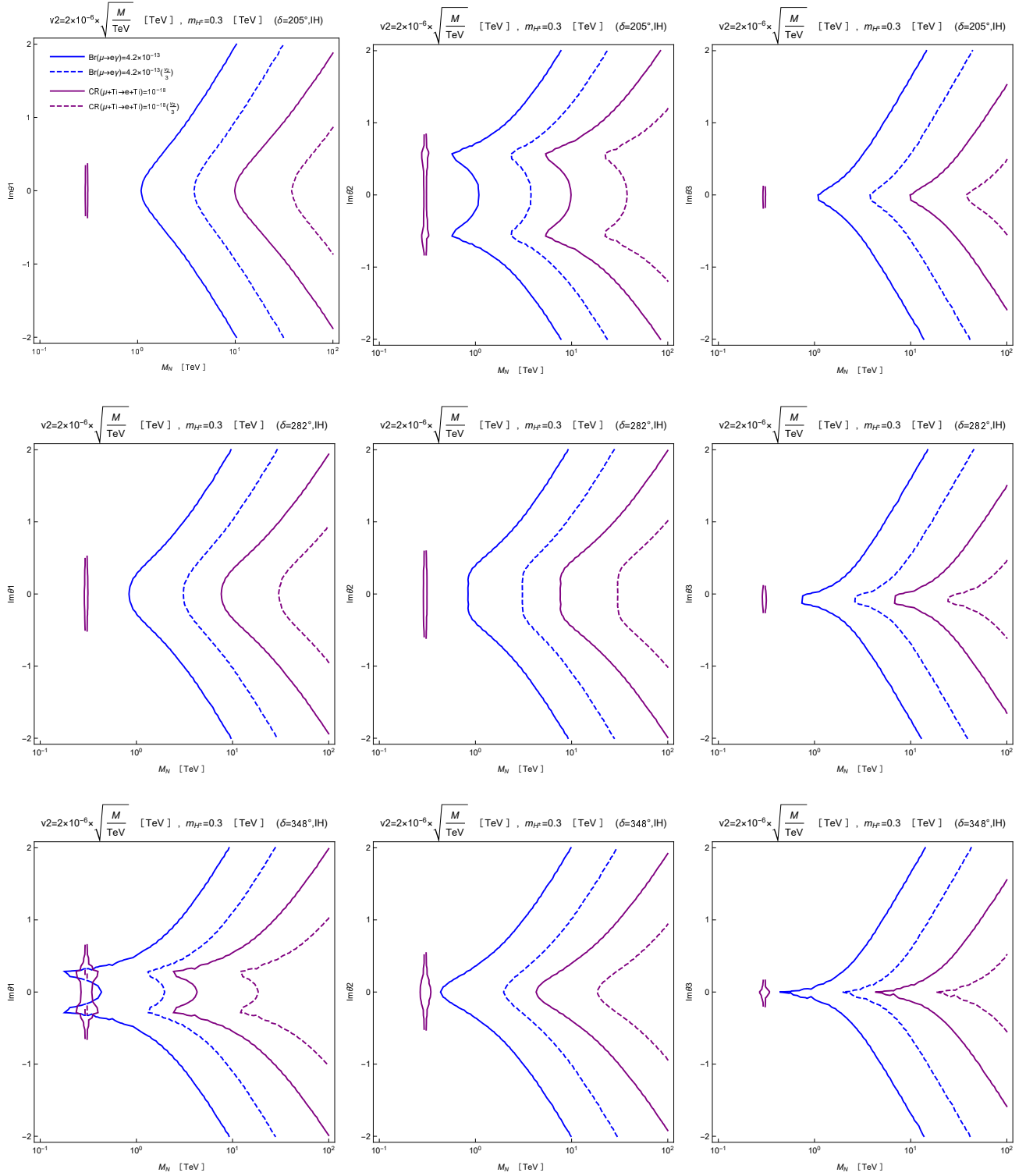


Fig. 11: Same as figure 10 except that mass hierarchy is Inverted Hierarchy and  $v_2$  is given in Eq. (44).

### 4.3.3 $Z \rightarrow \bar{e}_\alpha e_\beta$

There are three modes,  $Z \rightarrow e\mu$ ,  $Z \rightarrow e\tau$  and  $Z \rightarrow \mu\tau$ . In Fig. 12, the solid green, orange and red lines correspond to the contours of  $Br(Z \rightarrow e\mu) = 10^{-16}$ ,  $Br(Z \rightarrow e\tau) = 10^{-16}$  and  $Br(Z \rightarrow \mu\tau) = 10^{-16}$ , respectively, for NH and  $v_2$  in Eq. (43). Figure 13 is the corresponding figure for IHand  $v_2$  in Eq. (44).

In the same figure, the dashed green, orange and red lines correspond to the contours of  $Br(Z \rightarrow e\mu) = 10^{-16}$ ,  $Br(Z \rightarrow e\tau) = 10^{-16}$  and  $Br(Z \rightarrow \mu\tau) = 10^{-16}$ , respectively, when  $v_2$  is multiplied by 1/3. Since the dipole and non-dipole operators  $A_D$  and  $A_{ND}$  are both proportional to  $Y_D^2$ , the branching ratios  $Br(\mu \rightarrow e\gamma)$  and  $Br(Z \rightarrow \bar{e}_\alpha e_\beta)$  both scale with  $1/v_2^4$ . Hence, the relative location of the contours of  $Br(\mu \rightarrow e\gamma)$  and  $Br(Z \rightarrow e\mu)$ ,  $Br(Z \rightarrow e\tau)$  and  $Br(Z \rightarrow \mu\tau)$  do not depend on  $v_2$ .

We observe that in all cases, all of the  $Z \rightarrow e\mu$ ,  $Z \rightarrow e\tau$  and  $Z \rightarrow \mu\tau$  decays can be detected at a rate of about  $10^{-16}$  even when the model satisfies the current experimental bound on  $Br(\mu \rightarrow e\gamma)$ . Unfortunately, the rate  $10^{-16}$  is much lower than the future sensitivity of a high-luminosity  $Z$ -factory proposed in Ref. [25].

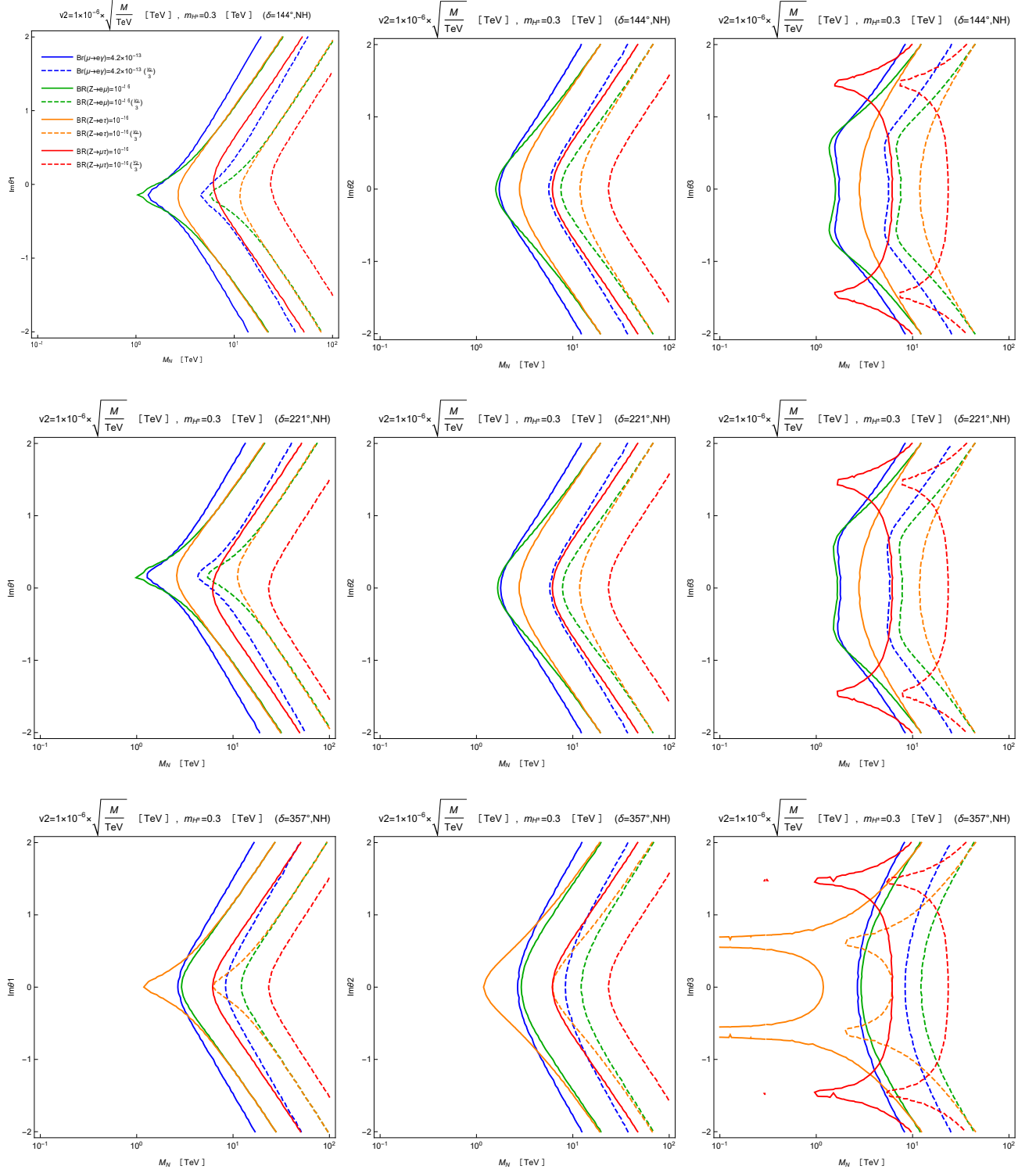


Fig. 12: Prediction for  $Br(Z \rightarrow e\mu)$ ,  $Br(Z \rightarrow e\tau)$  and  $Br(Z \rightarrow \mu\tau)$ , along with the values of  $Br(\mu \rightarrow e\gamma)$ . The neutrino mass hierarchy is Normal Hierarchy, and we fix  $m_{H^\pm} = 0.3$  TeV. We take  $\delta = 144^\circ$ ,  $221^\circ$  and  $357^\circ$  in the first, second and third rows. In the first column, we vary  $Im\theta_1 \neq 0$  while fixing  $Im\theta_2 = Im\theta_3 = 0$ . In the second column, we vary  $Im\theta_2 \neq 0$  while fixing  $Im\theta_1 = Im\theta_3 = 0$ . In the third column, we vary  $Im\theta_3 \neq 0$  while fixing  $Im\theta_1 = Im\theta_2 = 0$ . The solid blue line corresponds to  $Br(\mu \rightarrow e\gamma) = 4.2 \times 10^{-13}$  for  $v_2$  in Eq. (43), and the region on the left of the solid blue line is excluded by the search for  $Br(\mu \rightarrow e\gamma)$ . The solid green, orange and red lines correspond to the contours of  $Br(Z \rightarrow e\mu) = 10^{-16}$ ,  $Br(Z \rightarrow e\tau) = 10^{-16}$  and  $Br(Z \rightarrow \mu\tau) = 10^{-16}$ , respectively, for  $v_2$  in Eq. (43). The dashed blue line corresponds to  $Br(\mu \rightarrow e\gamma) = 4.2 \times 10^{-13}$  and the dashed green, orange and red lines correspond to the contours of  $Br(Z \rightarrow e\mu) = 10^{-16}$ ,  $Br(Z \rightarrow e\tau) = 10^{-16}$  and  $Br(Z \rightarrow \mu\tau) = 10^{-16}$ , respectively, when  $v_2$  is multiplied by  $1/3$ .

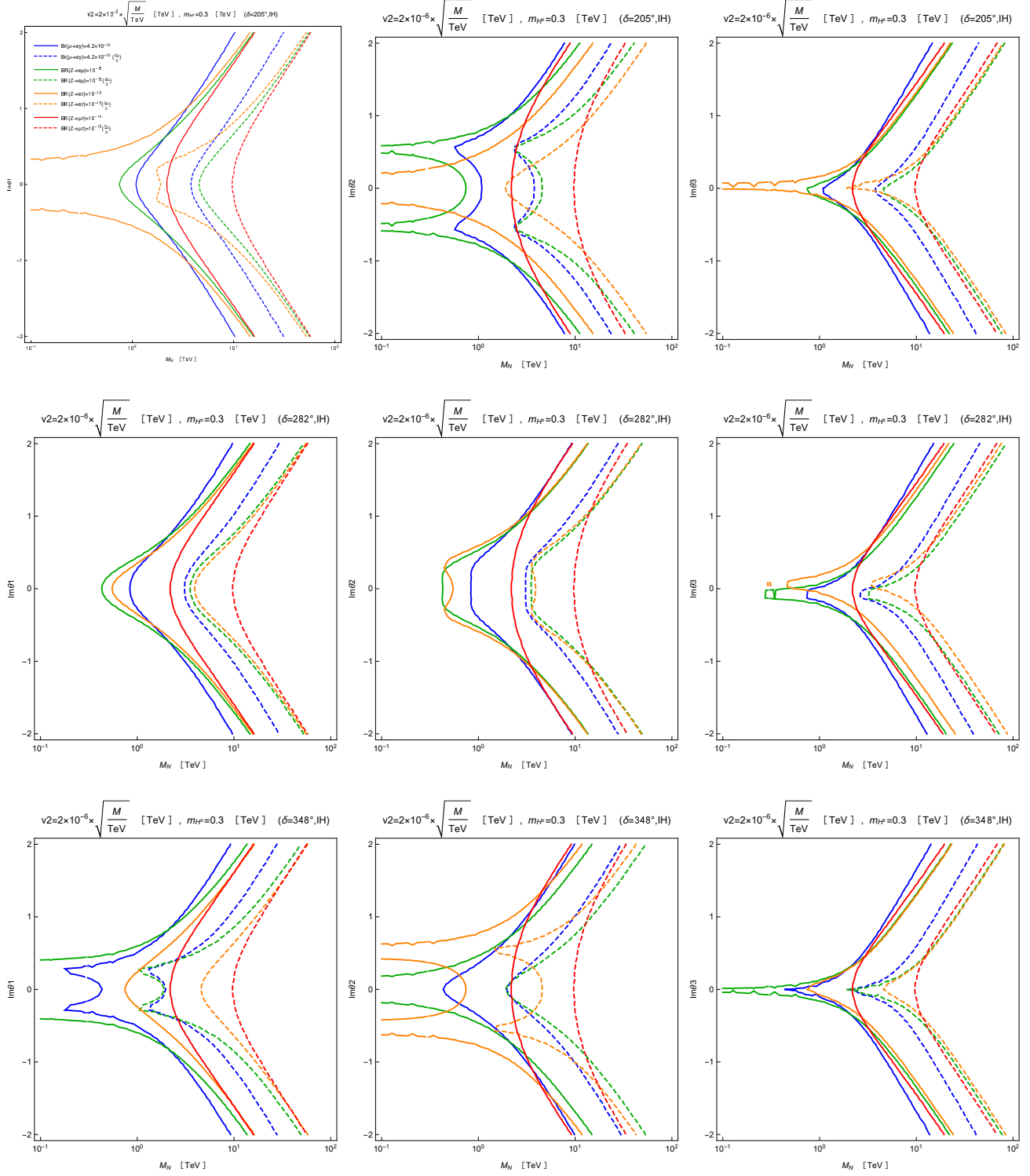


Fig. 13: Same as figure 12 except that the neutrino mass hierarchy is Inverted Hierarchy and  $v_2$  is given in Eq. (44).



#### 4.3.4 $h \rightarrow e\tau$ and $h \rightarrow \mu\tau$

Among the  $h \rightarrow \bar{e}_\alpha e_\beta$  ( $\alpha \neq \beta$ ) decay modes, the diagrams of  $h \rightarrow e\tau$  and  $h \rightarrow \mu\tau$  involve the large  $\tau$  Yukawa coupling and so these modes have much larger branching ratios than  $h \rightarrow e\mu$ . Therefore, we concentrate on the former two.  $Br(h \rightarrow e\tau)$  and  $Br(h \rightarrow \mu\tau)$  involve one unknown coupling constant, that is,  $\lambda_3$ . We present our prediction by assuming  $\lambda_3 = 1$ . Since the prediction scales with  $\lambda_3^2$ , it is straightforward to consider cases with other values of  $\lambda_3$ .

In Fig. 14, the solid green and orange lines correspond to the contours of  $Br(h \rightarrow e\tau)/Br(h \rightarrow \tau\tau) = 10^{-12}$  and  $Br(h \rightarrow \mu\tau)/Br(h \rightarrow \tau\tau) = 10^{-11}$ , respectively, for NH and  $v_2$  in Eq. (43). In the same figure, the dashed green and orange lines correspond to the contours of  $Br(h \rightarrow e\tau)/Br(h \rightarrow \tau\tau) = 10^{-12}$  and  $Br(h \rightarrow \mu\tau)/Br(h \rightarrow \tau\tau) = 10^{-11}$ , respectively, when  $v_2$  is multiplied by  $1/3$ .  $Br(\mu \rightarrow e\gamma)$  and  $Br(Z \rightarrow \bar{e}_\alpha e_\beta)$  ( $\alpha \neq \beta$ ) both scale with  $1/v_2^4$ , and so the relative location of their contours does not depend on  $v_2$ .

Figure 15 is the corresponding figure for IH and  $v_2$  in Eq. (44). Here, the green lines correspond to  $Br(h \rightarrow e\tau)/Br(h \rightarrow \tau\tau) = 10^{-13}$  and the orange lines correspond to  $Br(h \rightarrow \mu\tau)/Br(h \rightarrow \tau\tau) = 10^{-12}$ .

We observe that for NH we can hope that the  $h \rightarrow e\tau$  decay is detected at a rate  $Br(h \rightarrow e\tau)/Br(h \rightarrow \tau\tau) \sim 10^{-12}$  and that the  $h \rightarrow \mu\tau$  decay is detected at a rate  $Br(h \rightarrow \mu\tau)/Br(h \rightarrow \tau\tau) \sim 10^{-11}$  even when the model satisfies the current experimental bound on  $Br(\mu \rightarrow e\gamma)$ . If IH is the correct mass hierarchy, both  $Br(h \rightarrow e\tau)$  and  $Br(h \rightarrow \mu\tau)$  roughly decrease by  $1/10$ . Unfortunately, the predicted rate is too small to explain the hint of  $h \rightarrow \mu\tau$  decay reported by CMS [26].

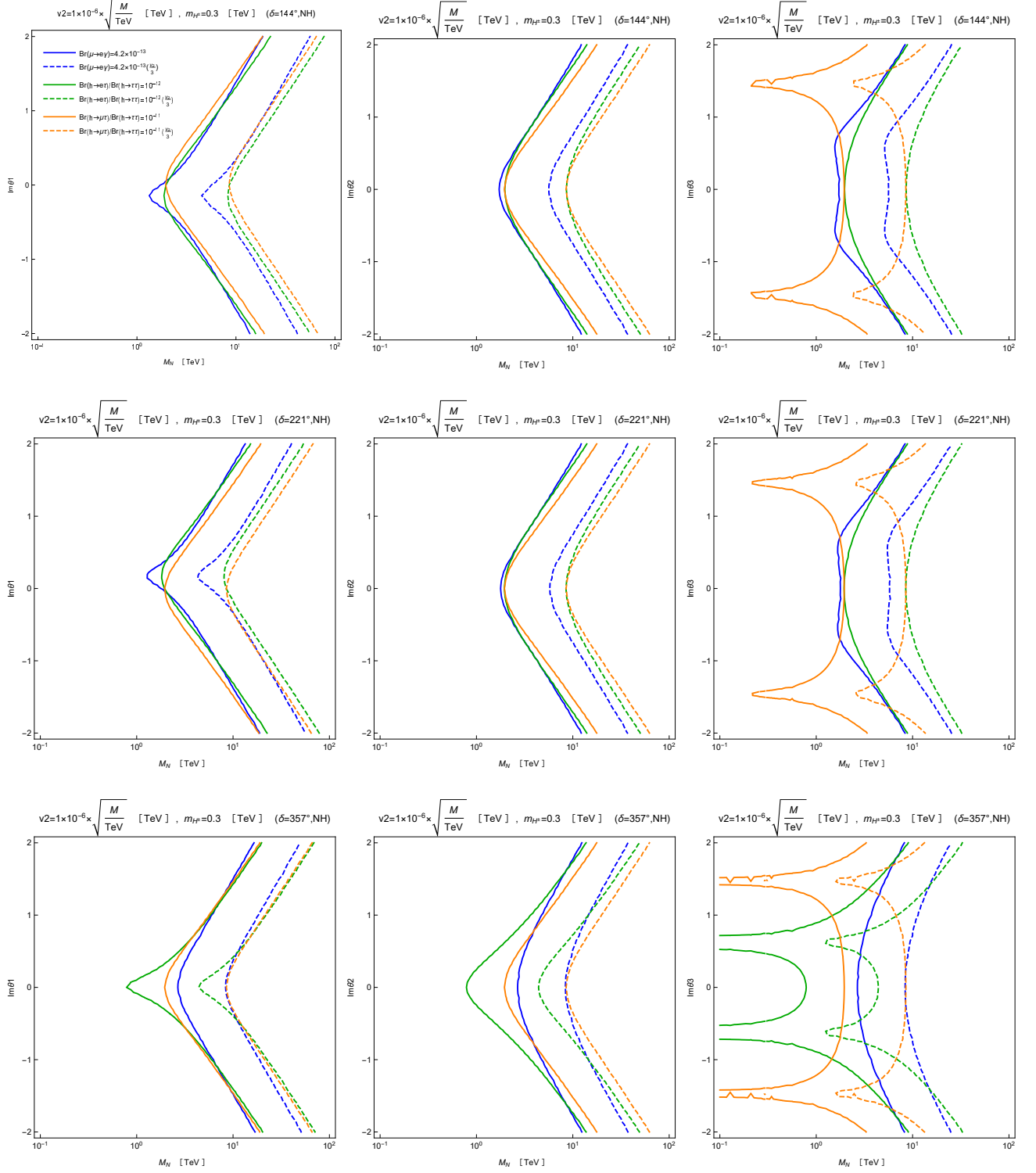


Fig. 14: Prediction for  $Br(h \rightarrow e\tau)$  and  $Br(h \rightarrow \mu\tau)$ , along with the values of  $Br(\mu \rightarrow e\gamma)$ . The neutrino mass hierarchy is Normal Hierarchy, and we fix  $m_{H^\pm} = 0.3$  TeV. We take  $\delta = 144^\circ$ ,  $221^\circ$  and  $357^\circ$  in the first, second and third rows. In the first column, we vary  $\text{Im}\theta_1 \neq 0$  while fixing  $\text{Im}\theta_2 = \text{Im}\theta_3 = 0$ . In the second column, we vary  $\text{Im}\theta_2 \neq 0$  while fixing  $\text{Im}\theta_1 = \text{Im}\theta_3 = 0$ . In the third column, we vary  $\text{Im}\theta_3 \neq 0$  while fixing  $\text{Im}\theta_1 = \text{Im}\theta_2 = 0$ . The solid blue line corresponds to  $Br(\mu \rightarrow e\gamma) = 4.2 \times 10^{-13}$  for  $v_2$  in Eq. (43), and the region on the left of the solid blue line is excluded by the search for  $Br(\mu \rightarrow e\gamma)$ . The solid green and orange lines correspond to the contours of  $Br(h \rightarrow e\tau)/Br(h \rightarrow \tau\tau) = 10^{-12}$  and  $Br(h \rightarrow \mu\tau)/Br(h \rightarrow \tau\tau) = 10^{-11}$ , respectively, for  $v_2$  in Eq. (43). The dashed blue line corresponds to  $Br(\mu \rightarrow e\gamma) = 4.2 \times 10^{-13}$  and the dashed green and orange lines correspond to the contours of  $Br(h \rightarrow e\tau)/Br(h \rightarrow \tau\tau) = 10^{-12}$  and  $Br(h \rightarrow \mu\tau)/Br(h \rightarrow \tau\tau) = 10^{-11}$ , respectively, when  $v_2$  is multiplied by  $1/3$ .

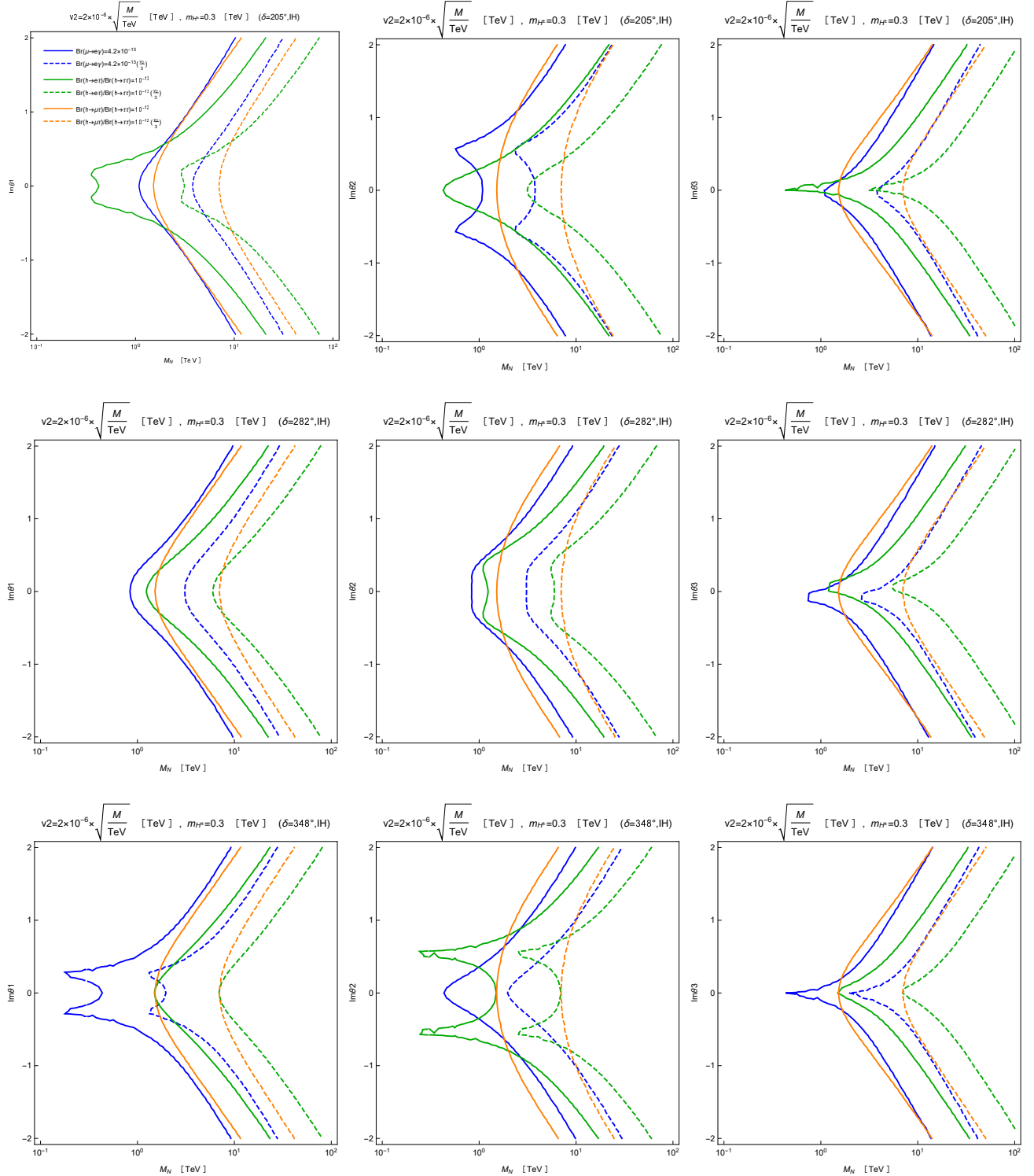


Fig. 15: Same as figure 14 except that the neutrino mass hierarchy is Inverted Hierarchy and  $v_2$  is given in Eq. (44) and that the solid green and orange lines correspond to the contours of  $Br(h \rightarrow e\tau)/Br(h \rightarrow \tau\tau) = 10^{-13}$  and  $Br(h \rightarrow \mu\tau)/Br(h \rightarrow \tau\tau) = 10^{-12}$ , respectively, and the dashed green and orange lines correspond to the contours of  $Br(h \rightarrow e\tau)/Br(h \rightarrow \tau\tau) = 10^{-13}$  and  $Br(h \rightarrow \mu\tau)/Br(h \rightarrow \tau\tau) = 10^{-12}$ , respectively, when  $v_2$  is multiplied by  $1/3$ .

## 5 Summary

We have investigated the neutrinophilic Higgs+seesaw model, in which right-handed neutrinos couple only with an extra Higgs field that develops a tiny VEV and have Majorana mass, and which realizes the low-scale seesaw naturally. We have concentrated on CLFV processes induced by loop diagrams of the charged scalar and heavy neutrinos. First, we have studied the current constraint on the model's parameter space from the search for  $\mu \rightarrow e\gamma$ . Secondly, we have predicted the branching ratios of other CLFV processes ( $\mu \rightarrow 3e$ ,  $\mu + \text{Al} \rightarrow e + \text{Al}$ ,  $\mu + \text{Ti} \rightarrow e + \text{Ti}$ ,  $Z \rightarrow e\mu$ ,  $Z \rightarrow e\tau$ ,  $Z \rightarrow \mu\tau$ ,  $h \rightarrow e\tau$  and  $h \rightarrow \mu\tau$ ), and discussed whether these processes can be detected in the future. An important finding is that, considering the future sensitivities, the  $\mu \rightarrow 3e$ ,  $\mu + \text{Al} \rightarrow e + \text{Al}$  and  $\mu + \text{Ti} \rightarrow e + \text{Ti}$  processes can be detected in a wide parameter region in the future, even when the model satisfies the current stringent bound on the  $\mu \rightarrow e\gamma$  branching ratio.

## Acknowledgment

This work is partially supported by Scientific Grants by the Ministry of Education, Culture, Sports, Science and Technology of Japan, Nos. 17K05415, 18H04590 and 19H051061 (NH), and No. 19K147101 (TY).

## Funding

Open Access funding: SCOAP.

## References

- [1] S. Gabriel and S. Nandi, Phys. Lett. B **655**, 141 (2007) [arXiv:hep-ph/0610253].
- [2] P. Minkowski, Phys. Lett. **67B**, 421 (1977).
- [3] T. Yanagida, Conf. Proc. C **7902131**, 95 (1979).
- [4] S. L. Glashow, NATO Sci. Ser. B **61**, 687 (1980).
- [5] R. N. Mohapatra and G. Senjanovic, Phys. Rev. Lett. **44**, 912 (1980).

- [6] E. Bertuzzo, Y. F. Perez G., O. Sumensari and R. Zukanovich Funchal, *JHEP* **01**, 018 (2016) [arXiv:1510.04284 [hep-ph]].
- [7] T. Toma and A. Vicente, *JHEP* **1401**, 160 (2014) [arXiv:1312.2840 [hep-ph]].
- [8] E. Ma, *Phys. Rev. D* **73**, 077301 (2006) [arXiv:hep-ph/0601225 [hep-ph]].
- [9] Z. Maki, M. Nakagawa and S. Sakata, *Prog. Theor. Phys.* **28**, 870 (1962).
- [10] B. Pontecorvo, *Sov. Phys. JETP* **7**, 172 (1958)
- [11] J. A. Casas and A. Ibarra, *Nucl. Phys. B* **618**, 171 (2001) [hep-ph/0103065].
- [12] M. E. Peskin and T. Takeuchi, *Phys. Rev. Lett.* **65**, 964 (1990)
- [13] M. E. Peskin and T. Takeuchi, *Phys. Rev. D* **46**, 381 (1992)
- [14] M. Tanabashi et al. [Particle Data Group], *Phys. Rev. D* **98**, no.3, 030001 (2018)
- [15] I. Esteban, M. C. Gonzalez-Garcia, A. Hernandez-Cabezudo, M. Maltoni and T. Schwetz, *JHEP* **1901**, 106 (2019) [arXiv:1811.05487 [hep-ph]].
- [16] I. Esteban, M. C. Gonzalez-Garcia, A. Hernandez-Cabezudo, M. Maltoni and T. Schwetz, *NuFIT 4.1* (2019) (available at [www.nu-fit.org](http://www.nu-fit.org), date last accessed June 30, 2020).
- [17] A. M. Baldini *et al.* [MEG Collaboration], *Eur. Phys. J. C* **76**, no. 8, 434 (2016) [arXiv:1605.05081 [hep-ex]].
- [18] B. Aubert *et al.* [BaBar Collaboration], *Phys. Rev. Lett.* **104**, 021802 (2010) [arXiv:0908.2381 [hep-ex]].
- [19] U. Bellgardt *et al.* [SINDRUM Collaboration], *Nucl. Phys. B* **299**, 1 (1988).
- [20] C. Dohmen *et al.* [SINDRUM II Collaboration], *Phys. Lett. B* **317**, 631 (1993).
- [21] W. H. Bertl *et al.* [SINDRUM II Collaboration], *Eur. Phys. J. C* **47**, 337 (2006).
- [22] A. Blondel *et al.*, arXiv:1301.6113 [physics.ins-det].
- [23] Y. Kuno [COMET], *PTEP* **2013**, 022C01 (2013)
- [24] E. Arganda, M. J. Herrero and A. M. Teixeira, *JHEP* **0710**, 104 (2007) [arXiv:0707.2955 [hep-ph]].

- [25] A. Abada, V. De Romeri, S. Monteil, J. Orloff and A. M. Teixeira, JHEP **1504**, 051 (2015) doi:10.1007/JHEP04(2015)051 [arXiv:1412.6322 [hep-ph]].
- [26] V. Khachatryan et al. [CMS], Phys. Lett. B **749**, 337 (2015) [arXiv:1502.07400 [hep-ex]].